Journal of Ultrafine Grained and Nanostructured Materials
https://jufgnsm.ut.ac.ir
Vol. 59, No.1, June 2026, pp. 27-40
Print ISSN: 2423-6845 Online ISSN: 2423-6837
DOI: 10.22059/jufgnsm.2026.01.03

Influence of friction surfacing parameters on microstructure and mechanical properties of AA1050 overlaid by AA6061-T6

Mohammad Javad Motekallem, Mahmoud Sarkari Khorrami*, Mahmoud Heydarzadeh Sohi

School of Metallurgy and Materials Engineering, College of Engineering, University of Tehran, P.O. Box 11155-4563, Tehran, Iran

Recieved: 29 May 2026; Accepted: 21 June 2026

**Corresponding author, E-mail:* m.khorrami@ut.ac.ir

ABSTRACT

This study investigates the friction surfacing (FS) of AA6061-T6 consumable rods onto AA1050 commercially pure aluminium substrates, focusing on the effects of rotational speed (1250–2500 rpm) and travel speed (250–750 mm/min) on coating geometry, microstructure, bond strength, and hardness. The results show that increasing either rotational or travel speed reduces both coating thickness and width due to enhanced material flowability and heat generation. Bond strength improves at higher rotational and travel speeds, attributed to greater viscoplastic flow and interfacial bonding. Optimum processing conditions produced a heat-affected zone (HAZ) approximately 2 mm deep in the substrate, with the central region and advancing side experiencing the most intense thermal exposure and recrystallisation. The central region exhibited coarser recrystallised grains due to prolonged heat exposure, while insufficient bonding occurred locally on both sides due to inadequate compressive force and material flow. Microhardness measurements revealed a 15% reduction in substrate hardness, mainly within the HAZ. Although strain hardening and dynamic recrystallisation in the deposited layer partially offset softening, the loss of T6 temper led to an overall 8% hardness reduction compared to the consumable rod. These findings demonstrate that FS process parameters critically govern coating dimensions, interfacial integrity, and mechanical performance.

Keywords: *Friction surfacing; Aluminum alloy; Consumable rod; Microstructure; Dynamic recrystallization.*

1. Introduction

Friction based solid state processes have sparked a considerable progress in the field of joining, welding, and surface engineering. Due to their unique process characteristics, theses processing routes can provide mechanical, metallurgical, and microstructural properties which are relatively difficult to achieve by other types of processes such as fusion based ones. As friction and plastic deformation constitute the sole heat sources, the process is conducted below the fusion temperature, thereby facilitating the joining of the substrate and deposited layer without complications associated with their intrinsic thermophysical properties [1-3].

The concept of friction surfacing (FS) was introduced first by Klopstock and Neelands in 1941, which is defined as a solid state procedure including a substrate and a deformable consumable metallic rod [4]. The process is based on an applied axial load pressing the rotating consumable rod against a substrate. The friction occurs at their interface produces local heating and generates a viscoplastic boundary layer at the tip of the rod, allowing it to move smoothly over the substrate while is being pressed by the axial load [5]. The linear movement leads to the deposition of a layer from the consumable rod on the substrate [6]. Given its layer-by-layer deposition capability, FS falls within the category of additive manufacturing, specifically known as friction stir additive manufacturing (FSAM) [7]. The main process parameters in FS are the travel speed, rotational speed, axial force, and the rod diameter.

In FS, a viscoplasticized solid state region is generated and processed into a new shape with its own unique properties. In this phenomenon, which is generally referred to as the ‘third-body region’ concept, the solid-state region demonstrates a three dimensional material flow pattern like a liquid, allowing easy mixing and blending between different materials. The solid-state region occurs at temperatures above the recrystallization temperature range and below the melting temperature of the material, offering relatively low flow stress. Therefore, the ‘third-body region’ is regularly used for improving joining of similar and dissimilar materials in the different friction-based variants [8, 9].

Although the process is almost free of metallurgical and physical defects which usually occur in fusion processes, the processed zones demonstrate some defects related to the process parameters such as unbonded edges on both the advancing side (AS) and retreating side (RS). They are also accompanied by constant generation of a revolving flash at the rod tip, which leads to the formation of a mushroom-shaped upset on the consumable rod [10].

Generally, the majority of investigations with regard to friction surfacing have focused on three areas: wear-resistant hard facing; anti-corrosion coatings; the manufacturing of long-life cutting tools; and the rehabilitation of corroded or damaged parts such as railways, turbine blades, and agricultural machinery [11]. Moreover, regarding the type of material, previous studies have mainly dealt with the deposition of ferrous alloys like tool steels, stainless steels, and mild steels, along with non-ferrous alloys such as copper- and nickel-based alloys. [12-14]. There are also a number of researches on light-weight alloys, specifically aluminum. In the deposition of heat-treatable aluminum alloys, the level of grain refinement and precipitate size and distribution mostly determine the properties of the deposited layer. Galviz et al. [15] investigated the process efficiency, the impact of various process parameters on mechanical properties, and interfacial bonding strength of interface in the deposition of AA5xxx onto AA6xxx aluminum alloys. Suhuddin et al. [16] addressed the recrystallization mechanisms on the FS of an AA6082-T6 aluminum alloy over AA2024-T3 by quantifying the microstructural evolutions at the consumable rod, with specific emphasis on the transition from the thermo-mechanically affected zone onto the fully recrystallized region. Sakihama et al. [17] deposited AA5052 aluminum alloy on the similar substrate and reported the impact of different parameters such as axial force and feeding rate on the width and tensile strength of the coated layer. In another work conducted by Tokisue et al. [18], the influence of the number of deposited layers on mechanical and microstructural properties of fabricated layer and the substrate in deposition of AA2xxx on AA5xxx aluminum alloys has been examined. According to their findings, the process efficacy for the double layer coating is obviously higher than that of the monolayer.

Nevertheless, given the growing demand for lightweight alloys in manufacturing and construction, investigations into the FS of AA1xxx aluminum alloys, particularly those focusing on microstructural behavior and mechanical properties, remain limited. The aim of the present work is to evaluate the feasibility of using AA1050 aluminum alloy as a substrate and AA6061-T6 aluminum alloy as a deposited layer in the FS process. Additionally, the study investigates the mechanical properties of both the substrate and the deposited layer through bending and microhardness tests.

Table 1- Chemical composition of AA1050 and AA6061 (the values are in weight percent)

Alloy	Chemical composition (wt. pct.)									
	Ti	Zn	Mn	Fe	Si	Mg	Cu	Cr	Others	Al
AA1050	0.05	0.05	0.03	0.35	0.25	0.04	0.05	-	-	balance
AA6061	0.12	0.18	0.12	0.55	0.4	1.1	0.25	0.3	0.05	balance

2. Materials and methods

2.1. Materials specification

AA1050 aluminum plates with a thickness of 8 mm and dimensions of 80 mm × 250 mm were used as substrates. The surfaces of the samples were ground with SiC sandpaper and cleaned by acetone prior to FS process. The chemical composition of AA1050 aluminum is given in Table 1. A rod with a diameter of 20 mm and length of 200 mm was cut from a 25 mm thick AA6061-T6 plate. The chemical composition is presented in Table 1. This rod was used as a consumable tool during the FS process.

2.2. Processing

As mentioned in the previous section, the consumable tool was 20 mm in diameter. The tool tilt angle and the applied force were fixed to 5° and 7 kN, respectively. The tilt angle improved materials deposition at the retreating side of the processed area as reported in [19, 20]. The FS process was carried out using the FP4M milling machine. The tip of the tool was cleaned by mechanical brush and acetone. Figs. 2(a) and (b) show the FS process and the fabricated specimen, respectively. Various combinations of rotational and travel speeds were selected to accomplish FS process as presented in Table 2. The parameters were determined through a series of preliminary trial-and-error experiments. These trials were conducted to identify a feasible processing window that would produce continuous, defect-free deposits while avoiding issues such as tool sticking, excessive flash formation, or insufficient bonding.

2.3. Materials characterization

The microstructural evolution of the processed specimen, as well as that of the consumable tool, was characterized under the optimal processing condition determined through the bending test. Longitudinal and cross-sectional samples of the tool, together with cross-sectional samples of the processed specimen, were prepared according to standard metallographic procedures. The specimens were then etched using a modified Keller's reagent for 90 s.

The bond strength between the deposited layer and the substrate was evaluated by a longitudinal bending test in accordance with the ASTM E290-09 standard [21], with the deposited layer subjected to tensile stress during testing. For this purpose, a three-point bending test setup with a crosshead speed of 0.042 mm/s was employed. Vickers microhardness measurements were performed from the substrate to the top of the deposited layer. The tests were conducted using an applied load of 50 gf and a dwell time of 15 s. Bend test and microhardness results were obtained as the average of three independent measurements taken from different locations on the specimen.

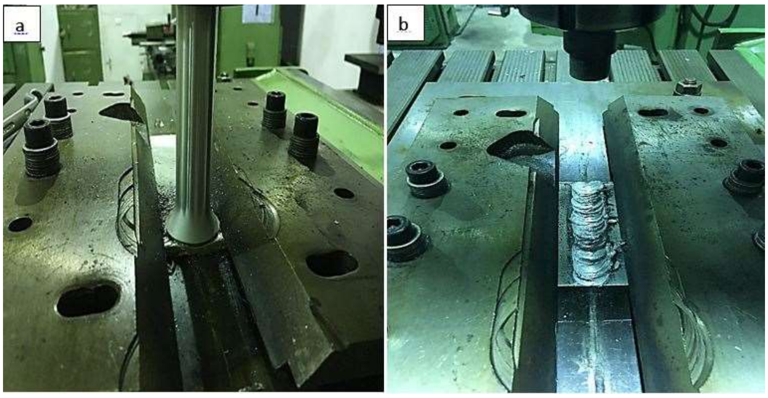

Fig. 1- (a) The FS process showing the plastic deformation at the tip of the consumable rod and (b) the processed specimen.

Table 2- FS process parameters

Sample	1	2	3	4	5	6	7	8
Rotational speed (rpm)	1250	1250	1600	1600	2000	2000	2500	2500
Travel speed (mm/min)	250	315	315	400	400	630	630	750

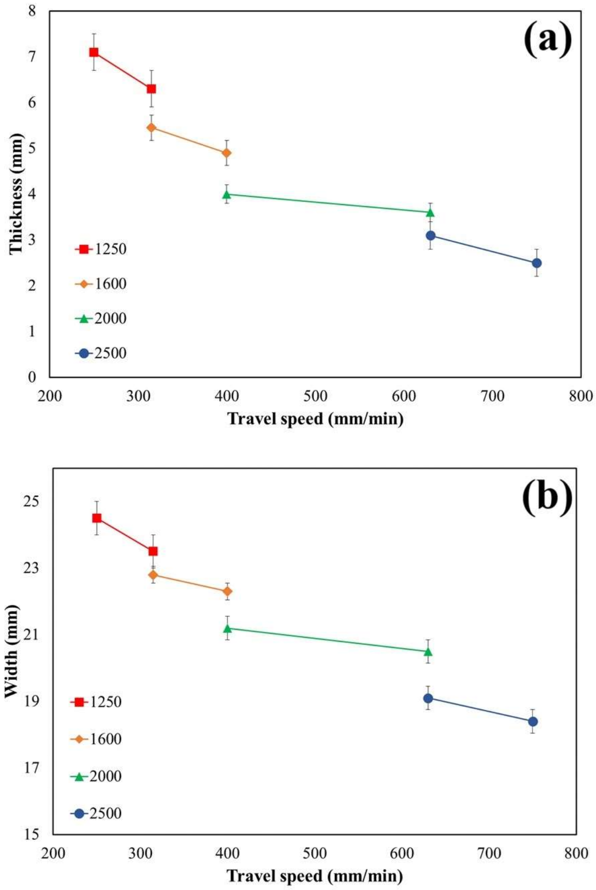

Fig. 2- Layer thickness (a) and width (b) variations as a function of travel speed at different rotational speeds: 1250, 1600, 2000, and 2500 rpm.

3. Results and discussion

3.1. Investigating the effect of process parameters

3.1.1. The effect of travel speed on layer geometry

In this study, the samples are divided into two groups based on the combination of rotational and travel speeds. The first group includes samples 1, 3, 5, and 7, which are deposited at rotational speeds of 1250, 1600, 2000, and 2500 rpm and travel speeds of 250, 315, 400, and 630 mm/min, respectively. According to Table 3, none of the samples share identical combinations of rotational and travel speeds. For instance, samples 5 and 6 both have a rotational speed of the 2000 rpm; however, their travel speeds differ, with sample 5 at 400 mm/min and sample 6 at 630 mm/min.

In contrast, samples 2, 4, 6, and 8 were processed at the same rotational speeds as those in the first group but at higher travel speeds. The effect of travel speed on the thickness and width of the deposited layer was investigated.

According to Fig. 2a, which illustrates the variation of layer thickness with travel speed, increasing the travel speed at a rotational speed of 1250 rpm (red line) reduces the deposited layer thickness. As demonstrated by Gandra et al. [22], the travel speed determines the rate at which material is deposited; therefore, a higher travel speed results in a thinner layer. In fact, increasing the travel speed reduces the time available for the material to bond with the substrate, thereby decreasing the amount of material deposited onto the substrate per unit time.

According to Fig. 2a, this procedure is repeated at all rotational speeds. At rotational speeds of 1600, 2000, and 2500 rpm, the thickness of the coating layer decreases with increasing the travel speed. Fig. 2b also shows changes in the width of the coating layer in terms of the travel speed at the constant rotational speed. It can be observed that, like the thickness of the coating layer, the width of the coating layer also reduces with increasing the travel speed.

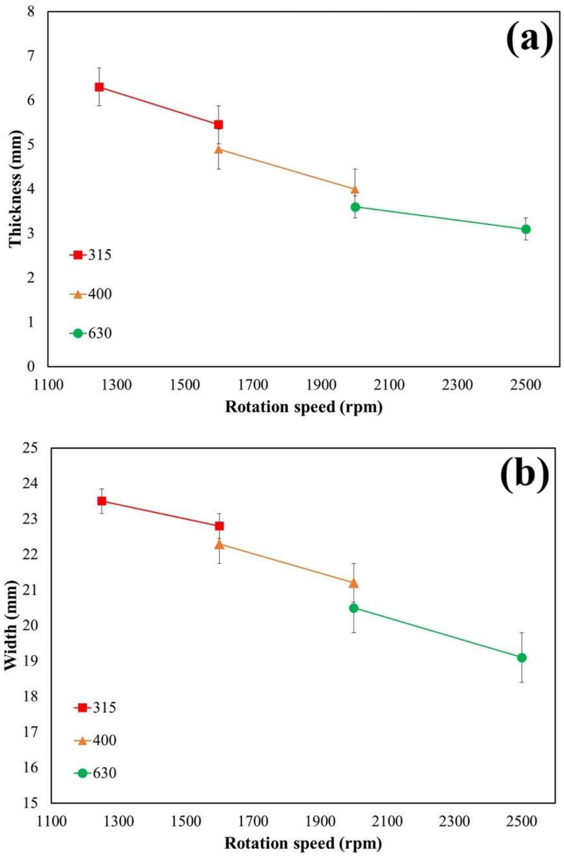

Fig. 3- Layer thickness (a) and width (b) variations as a function of rotational speed at different travel speeds: 315, 400, and 630 mm/min.

Table 3- Rotational and travel speeds of the samples in groups 1 and 2

Group 1			Group2		
Sample	ω (rpm)	V(mm/min)	Sample	ω (rpm)	V(mm/min)
1	1250	250	2	1250	315
3	1600	315	4	1600	400
5	2000	400	6	2000	630
7	2500	630	8	2500	750

3.1.2. The effect of rotational speed on layer geometry

Fig. 3 indicates variations in the thickness of the coating layer as a function of rotational speed. It can be observed that at constant travel speeds of 315, 400, and 630 mm/min (red, yellow, and green lines, respectively), increasing the rotational speed decreases the thickness of the coating layer. Additionally, Fig. 3 shows that at a constant travel speed, the width of the coating layer decreases as rotational speed increases. As declared by Akram et al. [23], this could be attributed to the variation of actual contact area between the consumable rod and the substrate during the FS process. The reason for simultaneous reduction of the width and thickness of the coating layer by increasing the rotational speed at constant travel speeds is that by increasing the rotational speed, the contact rate of the rod consumed with the substrate surface increases and as a result, the heat generated by friction between the consumable rod and the substrate also increases. As a result, the viscoplastic layer formed at the tip of the rod, due to higher temperature, is closer to the liquid phase and has more fluidity, resulting in less width and thickness and a much better bond quality [24]. In fact, high thicknesses at low rotational speeds also arise from this issue. Because of the less heat generated in the bonding interface, the material quickly converts from viscoplastic to solid and does not have enough time to flow. This trend was also observed in [25, 26] examining the FS of AA6xxx aluminum alloys.

3.2. Investigation of bond strength by bending test

Fig. 4 shows the appearance of the processed samples after the bending test. A three-point bending test was performed, and force was applied until the deposited layer separated from the substrate. As soon as the layer detached due to shear stress, the test was stopped, and the corresponding data were recorded. In fact, after the layer detaches, the material undergoes a type of yielding that reduces the applied force, resulting in a negative slope in the force-displacement curve.

Fig. 5 presents the force-displacement curves of the samples during the bending test. It can be observed that as the rotational and travel speeds of the process increase, the applied force required to rupture the bond—in other words, the bond strength—also increases. According to Figs. 4 and 5, sample 8, which has the highest rotational and travel speeds, exhibits the greatest bond strength and the highest deformation rate.

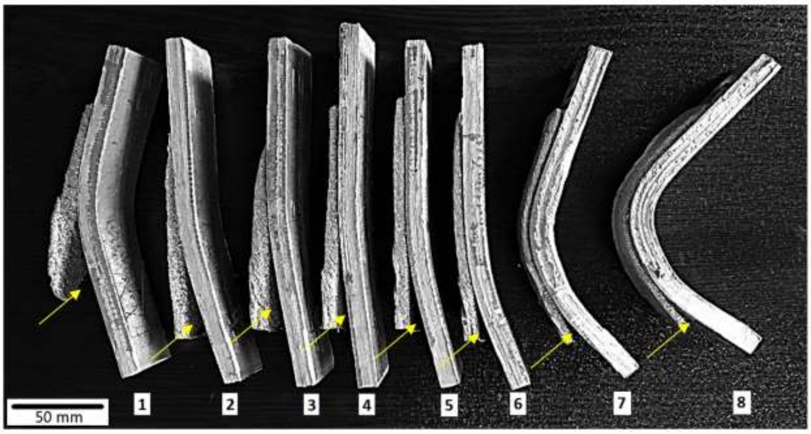

Fig. 4- Appearance of FS-processed samples after the bending test. Detachment of the deposited layer from the substrate demonstrates poor sample quality. The related defects are shown by arrow.

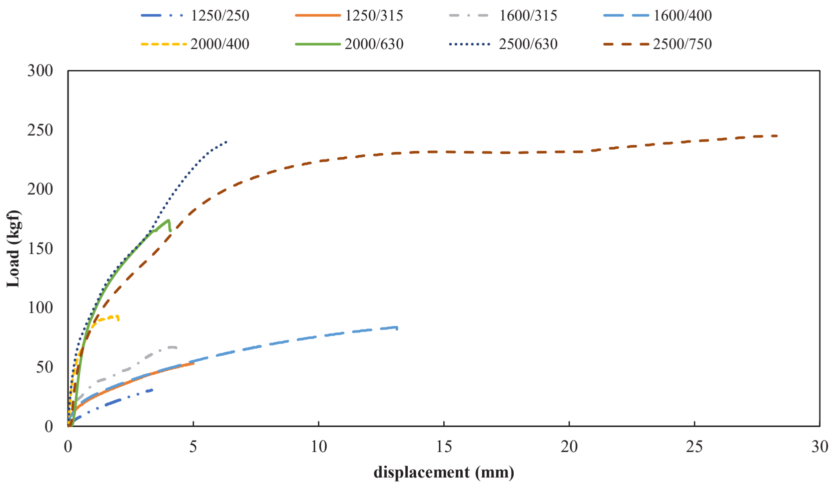

Fig. 5- Force-displacement curves obtained with the bending test for FS samples fabricated by various process parameters.

It was already mentioned that at higher rotational speeds, the viscoplastic material has greater fluidity, and this causes more plastic deformation in samples with higher rotational and travel speeds. In addition, friction-induced heat increases the temperature of the aluminum and provides enough heat for recrystallization in the deposited layer. On the other hand, mechanical locks created in the structure due to severe plastic deformation inhibit grain growth, and consequently, a fine grain structure with high toughness is formed. This fine-grained structure, which has high ductility, allows the layer to bend like a substrate with high ductility while simultaneously exhibiting high strength due to the fine grain structure resulting from severe plastic deformation. A similar trend has been reported by Pirhayati et al. [27], showing that increasing the rotational and travel speeds of the process results in higher plastic strain rates in the deposited layer.

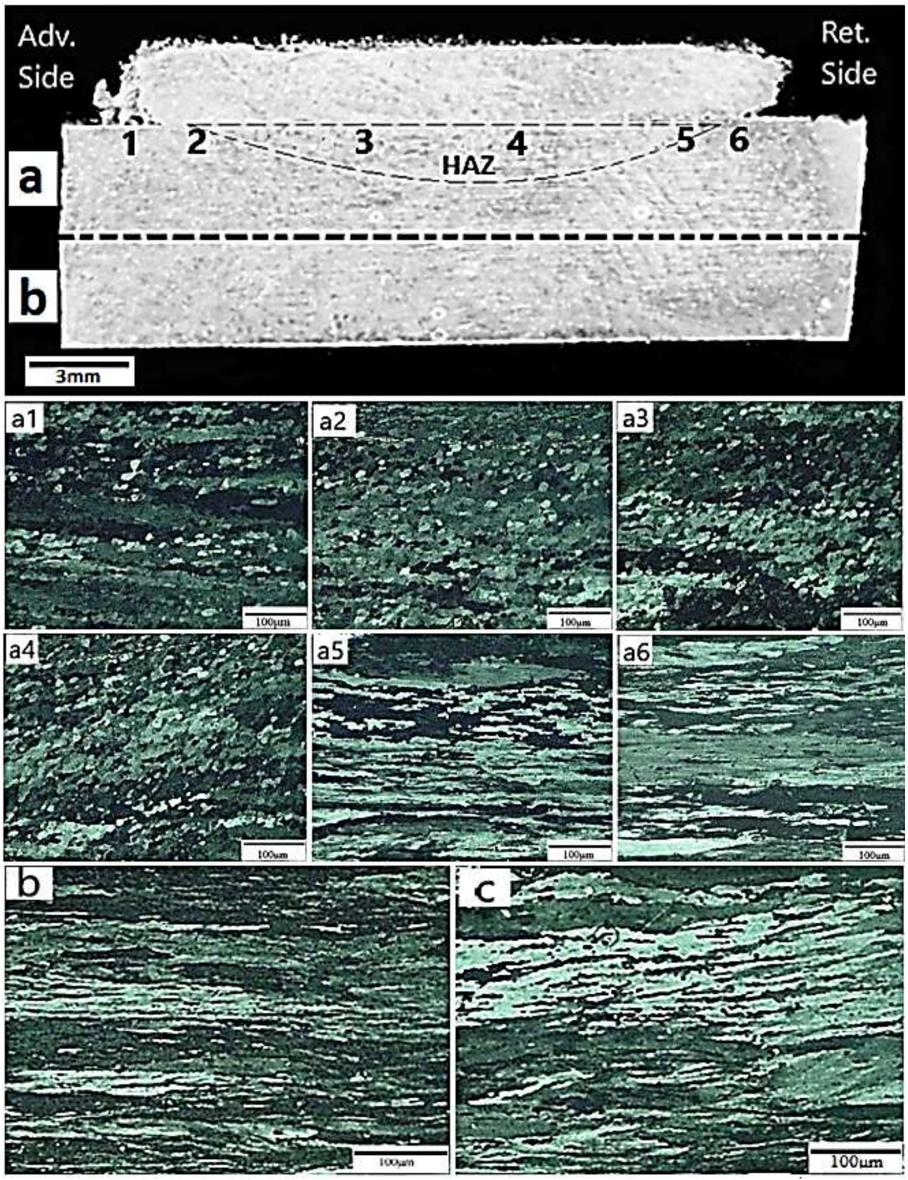

Fig. 6- Transverse cross-sectional images of the treated sample, together with the microstructures of different zones of the AA1050 aluminum substrate after the FS process: (a1–a5) areas affected either thermally or thermomechanically, whereas (b) and (c) are regions far from the interface.

As can be seen in Fig. 4, the samples deposited with lower rotational and travel speeds have a smaller bending angle, such that in samples 1 to 5, the coating layers are almost not bent. This is because the coating layer itself undergoes T6 heat treatment and has high strength and hardness, and severe plastic deformation also increases the hardness slightly. As a result, if the consumable rod is not completely recrystallized, it has high hardness and little flexibility and cannot withstand bending deformation. On the other hand, bond strength is low due to incomplete flow of the viscoplastic material, and no strong bond is established during the interaction process between the substrate and the consumable layer. Consequently, during the bending test, samples with lower rotational and travel speeds experience bond rupture.

3.3. Microstructural investigation

3.3.1. Substrate

Fig. 6 shows the cross-sectional images and magnified microstructures of different areas of sample 8. Fig. 6b shows the microstructure of the almost unaffected zone of the substrate during the deposition process. Fig. 6c also indicates the microstructure of material at the middle of the border of zone (a) and (b). According to Fig. 6b, there is no significant change in grain size, which is expected due to the distance from the interface.

In the FS process, the substrate temperature in aluminum alloys reaches the level required for recrystallization, given that the AA1050 was in the rolled condition [28]. Comparing Figs. 6a1 and a2 (advancing side) with Figs. 6a5 and a6 (retreating side) shows that the advancing side exhibits more microstructural changes in terms of recrystallization and grain growth. This observation is associated with greater heat generation at the advancing side, where the contact area between the consumable rod and the substrate is larger compared to the retreating side. On the retreating side, grains similar to those of the original substrate are observed; however, equiaxed grains have grown locally in some areas. The average grain size was measured to be 11 ± 2 μm in the advancing region, 24 ± 2 μm in the retreating region, and approximately 7 ± 2 μm in the central region (regions 3 and 4).

3.3.2. Deposited Layer

Fig. 7 shows the microstructure of the consumable rod before the FS process, consisting of equiaxed grains with varying sizes. The average grain size of the rod was about 28±2 μm. Fig. 8 shows the microstructure of different areas of the deposited layer after the process. The layer is divided into three distinct regions along the thickness. As reported in previous researches [6, 8, 10], due to the thermomechanical impacts of the FS process, grains are recrystallized, resulting in the grain refinement of the layer. As is evident in all figures, the processes of dynamic recrystallization and grain nucleation have been completely carried out due to the hot working and severe plastic deformation. This is responsible for the formation of a homogeneous and fine microstructure with a grain size of about 6±1.5 μm.

According to Fig. 8, in zone "a", which shows the upper surface of the deposited layer, the microstructure is finer compared with those of the other areas. The upper part of the deposit experiences the lowest amount of friction-induced heat during the process. In fact, once the recrystallization process is fully completed, the temperature in this region drops rapidly, leaving no time for grain growth. These temperature and stress conditions create a fine and homogeneous structure on the surface of the deposit. It was also reported by Rahmati et al. [29] that the upper part of the coating experiences the highest thermomechanical grain refinement.

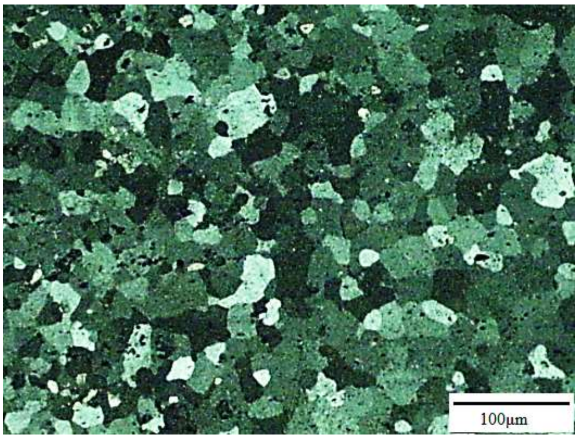

Fig. 7- Microstructure of the consumable rod before the FS process.

In zone “b”, which includes the middle part of the deposit, the microstructure has completely undergone recrystallization and subsequent grain growth. In zone “c”, which is located just above the interface, grains are coarser than those in zones “a” and “b”. This is due to proximity to the interface, which is the heat production center; this area remains viscoplastic for longer periods of time, and due to higher heat input, the recrystallized grains have more time to grow. Also, Figs. 8c1 and 8c3 show the microstructure in zone “c” on the advancing and retreating sides, respectively. According to the figures, in both the advancing and retreating regions, homogeneous and modified microstructures with fine grains can be observed. However, in the retreating region, the effect of plastic deformation remains evident in the recrystallized grains, and complete structural homogenization has not fully occurred in some areas due to the lower heat input.

3.3.3. Interface

Fig. 9 shows the microstructure of the interface between the substrate and the deposited layer, taken at the middle of the sample. Figs. 10 and 11 also show microstructures of the interface at the advancing and retreating sides, respectively. As illustrated in Figs. 9a and 9b, the deposited layer in the central region of the interface exhibits a significantly finer structure than that of the substrate. This refinement is attributed to the combined effects of frictional heat input and severe plastic deformation induced by compressive and shear forces, which promote dynamic recrystallization of the AA6061-T6 aluminum grains, thereby resulting in a homogeneous fine-grained microstructure. Similar trend is reported by Yu et al. [30] as well. In contrast, the substrate is primarily affected by heat input, leading to static recrystallization and subsequent grain growth as mentioned earlier. Moreover, the presence of sufficient compressive force in the central region facilitates complete metallurgical bonding between the substrate and the deposited layer. Consequently, the bonding interface is fully consolidated and free from porosity, cracks, and voids, as observed in Figs. 9c and d. Similar observation was reported by Gandra et al. [10].

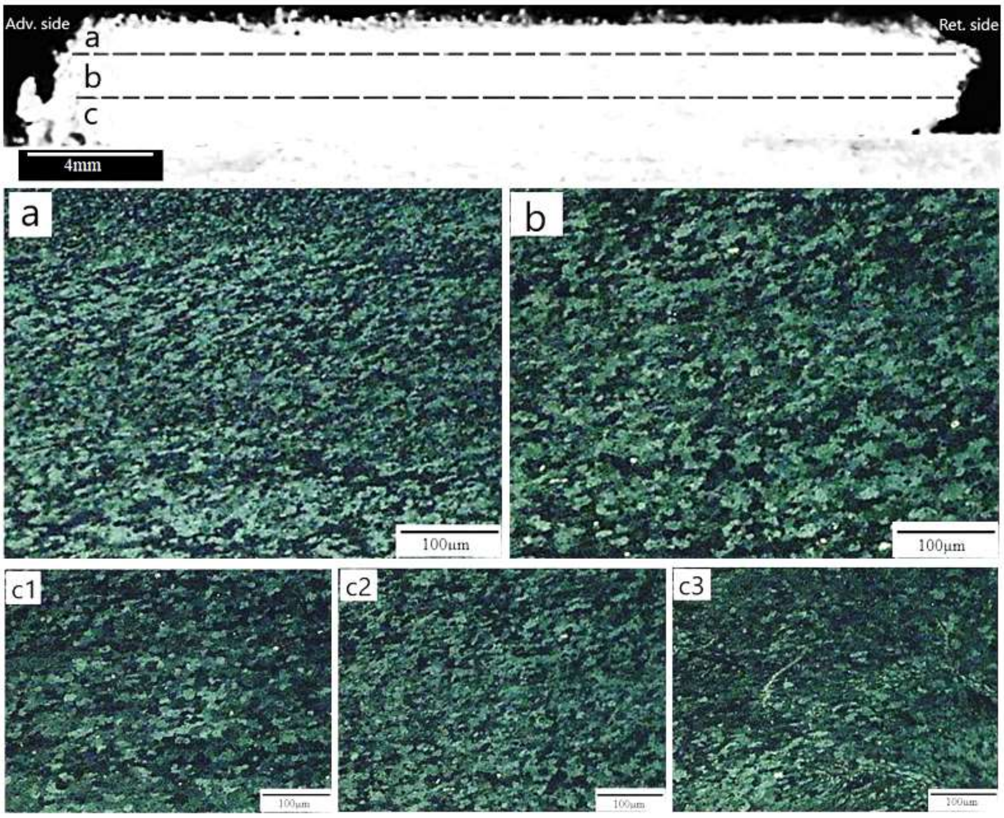

Fig. 8- Microstructure of various areas of the deposited layer: (a) top zone a; (b) middle zone b; (c1) advancing side of the bottom zone c; (c2) central region of the bottom zone c; (c3) retreating side of the bottom zone c.

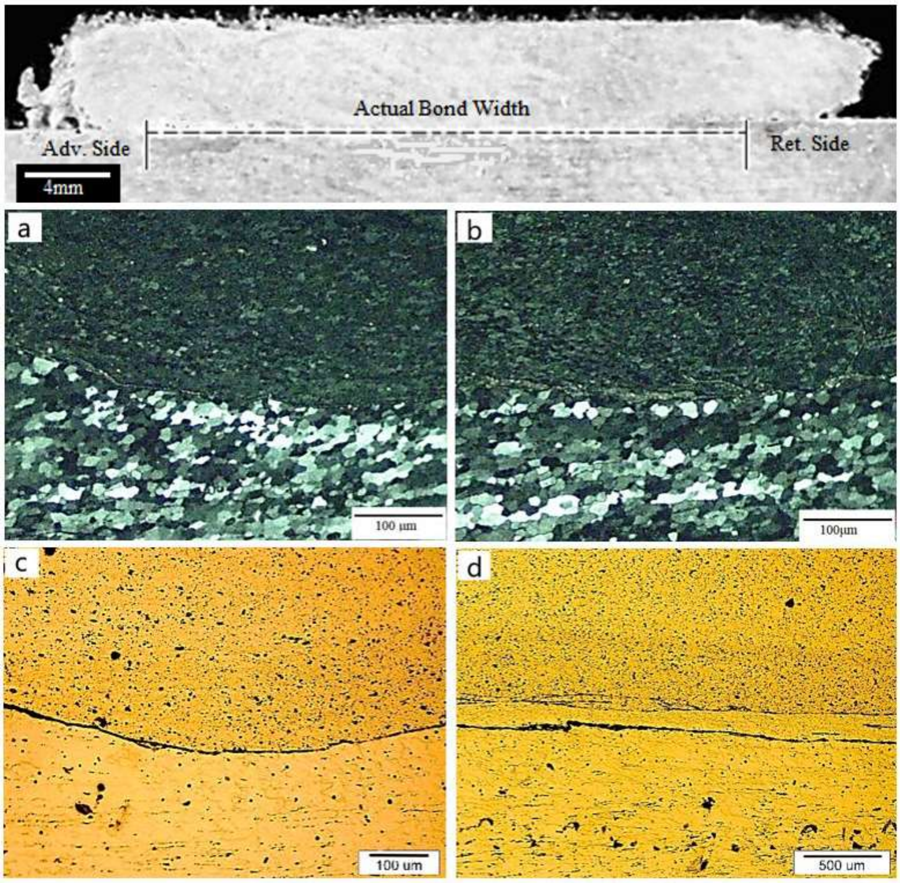

Fig. 9- Microstructure of the central regions of the bond interface under (a, b) polarized light and (c, d) conventional (bright-field) light conditions.

According to Figs. 10a and b, it can be observed that dynamic recrystallization occurs completely in the advancing area, however, the lack of sufficient compressive force at the edges has caused areas with weaker bonding at the edges (Figs. 10c and d). There are also cracks in parts of the advancing side. Fig. 10e shows a region of the interface in the advancing side where the crack has grown and Fig. 10f shows the same area with a higher magnification. One factor promoting crack growth in the AA6061-T6 deposition is the T6 heat treatment, which enhances the alloy's strength and brittleness. Consequently, the rod becomes more prone to cracking in areas with weak bonding, cavities, or stress concentrators when subjected to severe plastic deformation during deposition—on both the advancing and retreating sides. On the retreating side, an additional issue arises: misalignment between rotational and travel speeds relative to the joint interface introduces surplus shear stress, creating further stress concentrators and exacerbating crack growth in that region. Fig. 11 shows that larger and more numerous cracks are formed on the retreating side and the adjacent central region. These cracks primarily initiate in areas where the bonding between the deposited layer and the substrate is relatively weak. The combined effects of voids, residual process-induced stresses, and insufficient interfacial bonding promote crack propagation in these regions. Nevertheless, dynamic recrystallization in this area appears to be fully developed. Therefore, crack propagation on both the retreating and advancing sides can be attributed to two main factors: (i) inadequate interfacial bonding at the edges combined with residual process-induced stresses, and (ii) the reduced ductility of the aluminum alloy resulting from the pre-applied T6 heat treatment, which decreases material flowability and increases susceptibility to crack initiation and propagation.

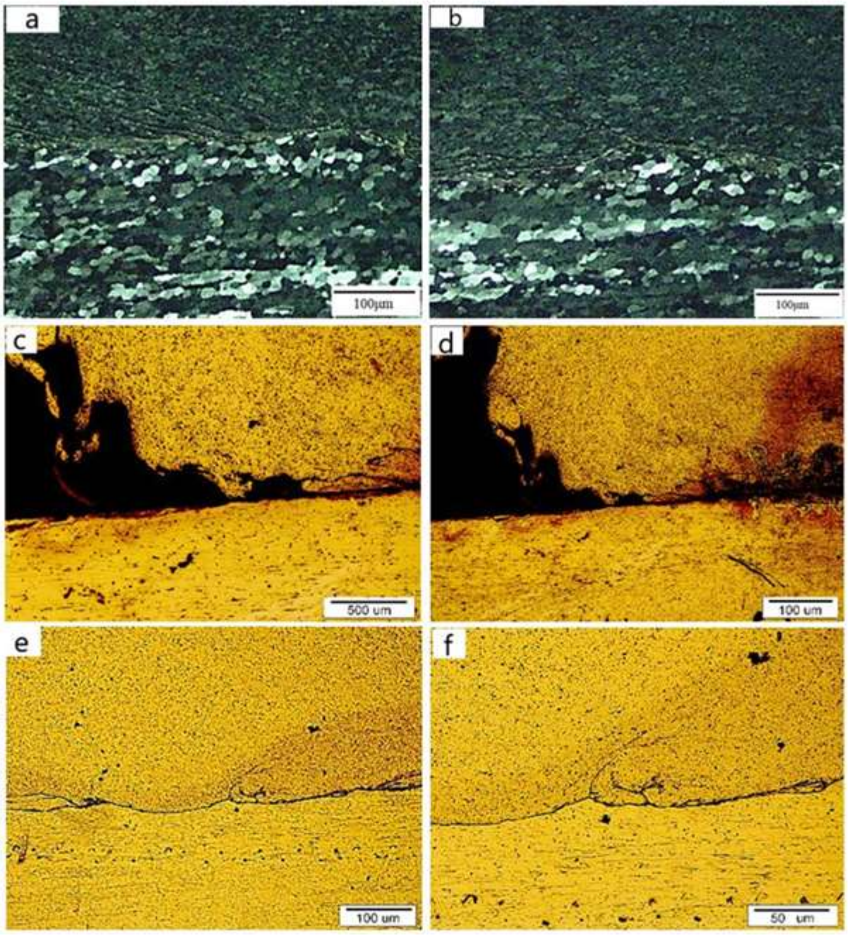

Fig. 10- (a,b) Microstructure of the interface on the advancing side of the processed sample. Interfacial cracks and debonding are shown under bright-field imaging: (c,d) edge of the deposited layer and (e,f) toward the central area.

3.4. Microhardness tests

Fig. 12 shows the cross section of the substrate, the deposited layer, and the rod after friction surfacing, which was prepared for microhardness measurements. Fig. 13 also indicates the relevant hardness profile along the distance. The initial hardness of the AA1050 aluminum substrate was measured at approximately 84 HV. At a distance of 2.2 mm from the interface, the substrate hardness begins to decrease, marking the extent of the heat-affected zone (HAZ). According to microhardness measurements, the HAZ length was approximately 2.2 mm. This reduction in hardness within the HAZ is caused by static recrystallization of the aluminum.

The hardness of the AA6061-T6 aluminum rod prior to the processing was approximately 104 HV. During the surfacing process, dynamic recrystallization, strain hardening, and severe plastic deformation contribute to hardness enhancement, whereas the loss of the T6 temper leads to hardness reduction. Similar occurrence was observed during additive manufacturing by FS of AA6061 [31]. The softening effect associated with the dissolution of the T6 heat treatment outweighs the strengthening effect induced by dynamic recrystallization and grain refinement. Consequently, the final hardness of the deposited layer was approximately 95 HV, representing an 8% decrease relative to the initial hardness. Similar drop in the hardness of the consumable rod was reported by Gandra et al. [10] in the FS of aluminum AA6082-T6 on aluminum AA2024-T3.

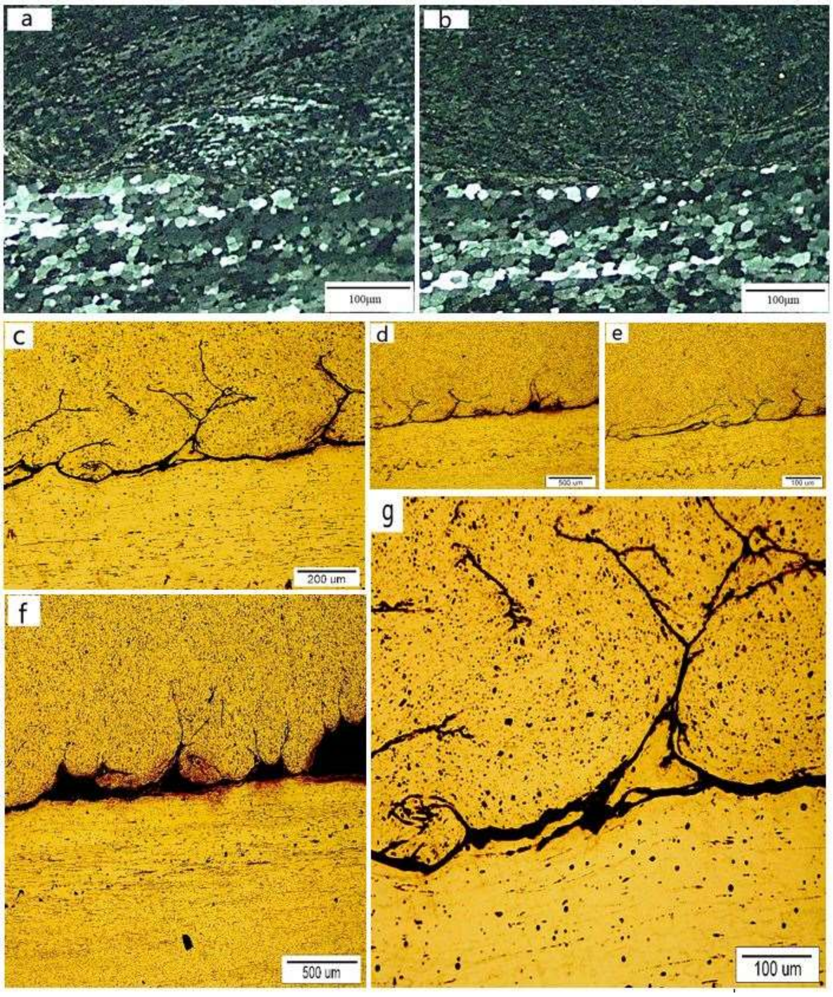

Fig. 11- (a,b) Microstructure of the interface on the retreating side of the processed sample. (c-g) Interfacial cracks and debonding are shown under bright-field imaging.

According to Fig. 13, the consumable rod after processing can be divided into three distinct regions. In the dynamically recrystallized (DR) zone, the material undergoes severe plastic deformation accompanied by strain hardening, complete dynamic recrystallization, and dissolution of precipitates. The hardness in this region was approximately 92 HV. In the second region, the rod experienced thermomechanical effects; however, dynamic recrystallization and strain hardening were not fully developed. Nevertheless, the T6 temper was completely lost in this zone, resulting in a lower hardness than that of the DR zone. The hardness in this region was measured to be approximately 83 HV. The third region, corresponding to the upper part of the consumable rod, was affected only by the loss of the T6 heat treatment and did not undergo significant thermomechanical deformation. Consequently, a reduction in hardness was also observed in this region. Overall, the results indicate that the hardness of the deposited layer decreased by approximately 12% after processing, whereas the substrate hardness decreased by approximately 15%.

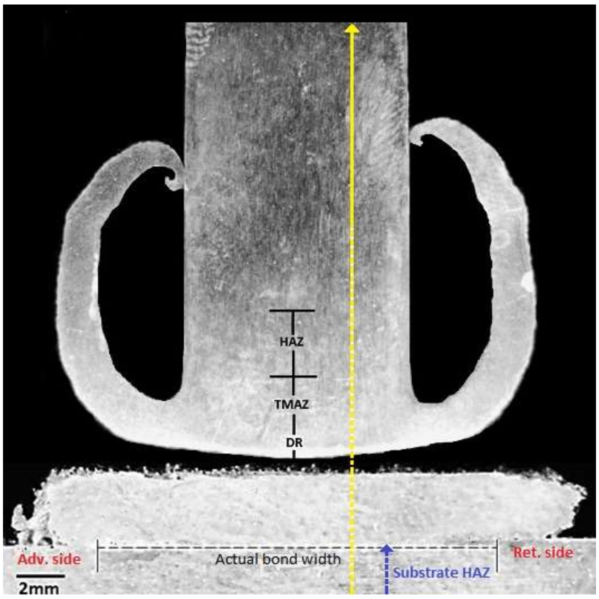

Fig. 12- Cross section of the substrate, deposited layer, and consumable rod after the FS process. Observed regions in the consumable rod: dynamically recrystallized (DR) zone, thermomechanically affected zone (TMAZ), and HAZ. The yellow line indicates the microhardness profile path.

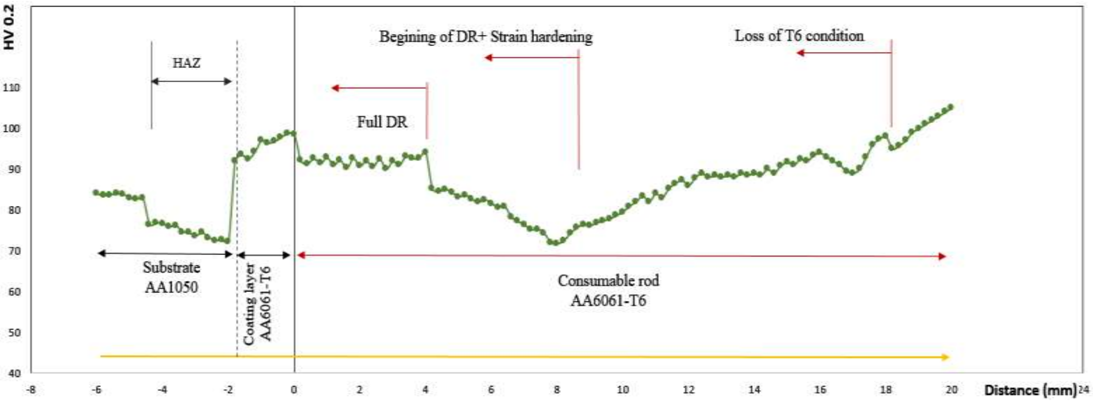

Fig. 13- Microhardness profile along the yellow line shown in Fig. 12, covering the substrate, deposited layer, and consumable rod.

4. Conclusions

Aluminum AA6061-T6 was successfully deposited on commercially pure aluminum AA1050 via the FS process under various rotational and travel speeds. The main findings are as follows:

- At constant rotational speeds, layer thickness and width decrease as travel speed increases. Similarly, at constant travel speeds, increasing rotational speed reduces layer thickness and width.
- Bond strength is directly influenced by rotational and travel speeds; increasing both parameters promotes viscoplastic material with higher flowability, resulting in enhanced bond strength.
- Under optimum processing conditions, a heat-affected zone (HAZ) formed to a depth of approximately 2 mm within the substrate. The central region of the deposited layer and the advancing side were most affected by heat input, as indicated by more extensive recrystallization.
- The central region of the deposited layer experienced the most pronounced microstructural changes due to its proximity to the heat generation zone. Owing to higher thermal exposure, recrystallized grains in this region underwent greater growth, resulting in a coarser microstructure. In contrast, insufficient bonding was observed in certain areas on both the

retreating and advancing sides due to inadequate compressive force and material flow.

- Substrate hardness decreased by approximately 15% after processing, with the most significant reduction in the HAZ. In the deposited layer, although strain hardening and dynamic recrystallization tend to increase hardness, the loss of the T6 pre-treatment during processing resulted in an overall hardness reduction of approximately 8% compared to the consumable rod.

References

1. Nicholas, E. D., & Thomas, W. M. (1998). A review of friction processes for aerospace applications. International Journal of Materials and Product Technology, 13(1-2), 45–55.
2. Gandra, J., Miranda, R. M., & Vilaça, P. (2012). Performance analysis of friction surfacing. Journal of Materials Processing Technology, 212(8), 1676–1686.
3. Gandra, J., Krohn, H., Miranda, R. M., Vilaça, P., Quintino, L., & Dos Santos, J. F. (2014). Friction surfacing—A review. Journal of Materials Processing Technology, 214(5), 1062–1093.
4. Klopstock, H., & Neelands, A. (1941). An improved method of joining or welding metals, Patent specification Ref 572789.
5. Chandrasekaran, M., Batchelor, A. W., & Jana, S. (1997). Friction surfacing of metal coatings on steel and aluminum substrate. Journal of Materials Processing Technology, 72(3), 446–452.
6. Galvis, J. C., Oliveira, P. H. F., Hupalo, M. F., Martins, J. P., & Carvalho, A. L. M. (2017). Influence of friction surfacing process parameters to deposit AA6351-T6 over AA5052-H32 using conventional milling machine. Journal of Materials Processing Technology, 245, 91–105.
7. Gholamzadeh-Sarmi, M. J., Fatemi, S.M., Mollaei, N., Abedi, A. (2024). Processing of Ultrafine/nano-grained microstructures through additive manufacturing techniques: a critical review. Journal of Ultrafine Grained and Nanostructured Materials, 57, 203–221.
8. Bararpour, S. M., Jamshidi Aval, H., & Jamaati, R. (2019). Modeling and experimental investigation on friction surfacing of aluminum alloys. Journal of Alloys and Compounds, 805, 57–68.
9. Rahmati, Z., Jamshidi Aval, H., Nourouzi, S., & Jamaati, R. (2021). Effect of mechtrode rotational speed on friction surfacing of AA2024 on AA1050 substrate. CIRP Journal of Manufacturing Science and Technology, 33, 209–221.
10. Gandra, J., Pereira, D., Miranda, R. M., Silva, R. J. C., & Vilaça, P. (2013). Deposition of AA6082-T6 over AA2024-T3 by friction surfacing - Mechanical and wear characterization. Surface and Coatings Technology, 223, 32–40.
11. Puli, R., & Janaki Ram, G. D. (2012). Wear and corrosion performance of AISI 410 martensitic stainless steel coatings produced using friction surfacing and manual metal arc welding. Surface and Coatings Technology, 209, 1–7.
12. Guo, D., Kwok, C. T., & Chan, S. L. I. (2019). Spindle speed in friction surfacing of 316L stainless steel – How it affects the microstructure, hardness and pitting corrosion resistance. Surface and Coatings Technology, 361, 324–341.
13. Silva, K. H. S., Brito, P. P., Santos, I. B., Câmara, M. A., & Abrão, A. M. (2020). The behaviour of AISI 4340 steel coatings on low carbon steel substrate produced by friction surfacing. Surface and Coatings Technology, 399, 126170.
14. Guo, D., Kwok, C. T., & Chan, S. L. I. (2018). Fabrication of stainless steel 316L/TiB2 composite coating via friction surfacing. Surface and Coatings Technology, 350, 936–948.
15. Galvis, J. C., Oliveira, P. H. F., Hupalo, M. F., Martins, J. P., & Carvalho, A. L. M. (2017). Influence of friction surfacing process parameters to deposit AA6351-T6 over AA5052-H32 using conventional milling machine. Journal of Materials Processing Technology, 245, 91–105.
16. Suhuddin, U., Mironov, S., Krohn, H., Beyer, M., & Santos, J. F. Dos. (2012). Microstructural Evolution During Friction Surfacing of Dissimilar Aluminum Alloys. Metallurgical and Materials Transactions A 2012 43:13, 43(13), 5224–5231.
17. Sakihama, H., Tokisue, H., & Katoh, K. (2003). Mechanical Properties of Friction Surfaced 5052 Aluminum Alloy. MATERIALS TRANSACTIONS, 44(12), 2688–2694.
18. Tokisue, H., Katoh, K., Asahina, T., & Usiyama, T. (2006). Mechanical properties of 5052/2017 dissimilar aluminum alloys deposit by friction surfacing. Materials Transactions, 47(3), 874–882.
19. Liu, S., Bor, T. C., Van Der Stelt, A. A., Geijselaers, H. J. M., Kwakernaak, C., Kooijman, A. M., … Van Den Boogaard, A. H. (2015). Friction surface cladding: An exploratory study of a new solid state cladding process. Journal of Materials Processing Technology, 229, 769–784.
20. Vitanov, V. I., & Voutchkov, I. I. (2005). Process parameters selection for friction surfacing applications using intelligent decision support. Journal of Materials Processing Technology, 159(1), 27–32.
21. ASTM E290 - 09 Standard Test Methods for Bend Testing of Material for Ductility, 10.1520/E0290-09.
22. Gandra, J., Pereira, D., Miranda, R. M., & Vilaça, P. (2013). Influence of Process Parameters in the Friction Surfacing of AA 6082-T6 over AA 2024-T3. Procedia CIRP, 7, 341–346.
23. Akram, J., Kalvala, P. R., & Misra, M. (2014). Effect of process parameters on friction surfaced coating dimensions. Advanced Materials Research, 922, 280–285.
24. Kallien, Z., Rath, L., Roos, A., & Klusemann, B. (2020). Experimentally established correlation of friction surfacing process temperature and deposit geometry. Surface and Coatings Technology, 397, 126040.
25. Kumar Sahoo, D., Nivas Chari, A., Sivakrishna Reddy, A. (2020). Optimization & characterization of friction surfaced coatings of AA6063 aluminium alloy over AISI316 stainless steel substrate. Materials Today: Proceedings, 23, 565–572.
26. S. Mohanasundaram, S., Vijay, S. J., Ajay Vasanth, X., Rai, R. S., Kantharaj, I. (2020). Optimization of coating thickness and coating width for friction surfaced Al6061-B4C over Al6061, Materials Today: Proceedings, 33, 939–945.
27. Pirhayati, P., Aval, H. J., (2019). An investigation on thermo-mechanical and microstructural issues in friction surfacing of Al–Cu aluminum alloys, Mater. Res. Express 6, 056550.
28. Sarkari Khorrami, M. (2021). Friction stir welding of ultrafine grained aluminum alloys: a review. Journal of Ultrafine Grained and Nanostructured Materials, 54, 1–20.
29. Rahmati, Z., Jamshidi Aval, H., Nourouzi, S., & Jamaati, R. (2021). Effect of friction surfacing parameters on microstructure and mechanical properties of solid-solutionized AA2024 aluminium alloy cladded on AA1050. Materials Chemistry and Physics, 269, 124756.
30. Yu, M., Zhang, Z., Zhao, H., Zhou, L., & Song, X. (2019). Microstructure and corrosion behavior of the ultra-fine grained aluminum coating fabricated by friction surfacing. Materials Letters, 250, 174–177.
31. Sharifi, A., Khodabakhshi, F., Kashani-bozorg, S. F., Gerlich, A. P. (2023). Microstructure and mechanical properties in additive manufacturing by friction surfacing of AA6061 alloy, 884, 145520.